NATIONAL AERONAUTICS AND SPACE ADMINISTRATION

Technical Memorandum 33-206

Solar Performance Evaluation Test Program of the 9.5-Ft-Diam. Electroformed Nickel Concentrator S/N 1 at Table Mountain, California

Floyd A. Blake

N67-31438
(ACCESSION NUMBER)

40
(PAGES)

(THRU)

7
(CODE)

CR #85750
(NASA CR OR TMX OR AD NUMBER)

23
(CATEGORY)

FACILITY FORM 602

JET PROPULSION LABORATORY
CALIFORNIA INSTITUTE OF TECHNOLOGY
PASADENA, CALIFORNIA

June 15, 1967

Technical Memorandum 33-206

Solar Performance Evaluation Test Program of the 9.5-Ft-Diam. Electroformed Nickel Concentrator S/N 1 at Table Mountain, California

Floyd A. Blake

Approved by:

P. Goldsmith, Manager
Spacecraft Power Section

Technical Memorandum 33-206

FOREWORD

This Report presents the results of one phase of research carried out at the Jet Propulsion Laboratory, California Institute of Technology, under Contract NAS 7-100, sponsored by the National Aeronautics and Space Administration.

The author, Floyd A. Blake, is an employee of the Missile and Space Division of the General Electric Company of Valley Forge, Pennsylvania. The work described in this Report was accomplished during his residence at the Jet Propulsion Laboratory under Contract BZ4-206764.

ACKNOWLEDGMENTS

CONTENTS

TABLES

FIGURES

FIGURES (Cont'd)

ABSTRACT

This Report presents the results of the optical and calorimetric tests performed on 9.5-ft-diam. nickel mirrors obtained by electroforming the metal on a master produced by the spincasting of epoxy plastic.

I. INTRODUCTION

A program to develop lightweight, high-quality paraboloidal solar concentrators capable of efficiently powering thermionic cavity generators is being pursued by the Jet Propulsion Laboratory. The design and fabrication of a 9.5-ft-diam., 45-deg-rim-angle, electroformed nickel male mirror master and a replica concentrator was awarded to General Electric Co., Spacecraft Department, on August 30, 1962, with the initiation of JPL Contract 950239.

The major steps in the fabrication sequence were:

1. Production of a female master by spincasting epoxy plastic.
2. Production of a male master by electroforming on the female master.
3. Production of the solar concentrator by electroforming on the male master.

The sample concentrator obtained from this male master is shown in Fig. 1 during installation into the solar tracker at the JPL Solar Test Facility atop Table Mountain, California, December 23, 1963.

The optical and thermal performance evaluation and calibration prior to integration of the mirror with a thermionic generator test system were performed by JPL during the months of January, February, and April 1964 at Table Mountain. Program steps included:

1. Strengthening of the solar tracker to enable rigid mounting of the 9.5-ft mirror and generator test system. The principal features of this strengthening were to convert the "ring" support of the mirror to an approximate "dome" structure, as shown in Fig. 2, and to add lateral supports to the focal-zone mount, completing a tripod.
2. Alignment of the tracking sensor control and the tracking telescope with the optical axis of the concentrator and positioning of the focal-zone aperture on the optical axis at the focal plane by use of the Hartman test equipment.
3. Optical inspection of the mirror by Hartman test. Data from 200 points on the mirror, equally distributed on the basis of equal area, were obtained and form the basis for the statistical

quality, contour map, and theoretical performance curves (variable reflectivity) used to correlate the optical and calorimetric results.

4. Calorimetric evaluation of the energy-collection capability of the mirror with variable concentration ratios, ranging from 6630 with the 1.400-in.-diam. aperture to 33,270 with the 0.625-in.-diam. aperture.

5. Calorimetric calibration of the energy loss resulting from the 1-in.-thick quartz window of the vacuum chamber used during the generator tests.

6. Calorimetric determination of the energy-collection performance reduction resulting from disorientation of the mirror optical axis from the Sun up to 12 min of arc in the High, Low, East, and West directions.

7. Calorimetric evaluation of the central 7.5-ft-diam. part of the mirror. This portion of the program was added when the optical inspection revealed a rather abrupt change in contour of the mirror near the 7.5-ft diameter, probably a distortion introduced during final processing or shipping operations. The results from the central zone were expected to more nearly approach quality limits attainable from the master than the overall results obtained from the full 9.5-ft diameter with regard to efficiency of the reflecting surface and minimization of geometrical error.

Detailed results of tests, standardized performance data, and analytical evaluation of the capability of the 9.5-ft-diam. electroformed mirror, S/N 1, form the remainder of this Report.

II. OPTICAL INSPECTION - MODIFIED HARTMAN TEST

A. HARTMAN TEST SETUP AND METHOD

The modified Hartman test is illustrated schematically in Fig. 3 and shown in operation in Fig. 4. It is an optical inspection test that permits the attainment of the detail geometric quality of a wide number of individual points distributed over the surface of the mirror. This technique is also used for alignment of the mirror's

optical axis with the Sun, and subsequently the alignment of the tracker control sensors and the monitoring telescope with the optical axis. Positioning of the focal-zone equipment is also controlled using the Hartman test equipment.

An opaque screen masks direct sunlight from the mirror. Individual holes, or groups of holes, in the screen are uncovered and the resulting images observed on the target. Individual image position data were observed for each of 200 points distributed uniformly over the mirror area. The paraxial-ray intercept point on the focal plane was established by the intersection of the major and minor ellipse axes. The tangential error was then determined analytically by trigonometry. Layout of the screen-hole pattern is such that each hole is centered in a 1/200th segment of the mirror area (51.03 in.^{2} per point). Ten holes at each of 20 angular positions are drilled. These are coded A to J starting from the innermost and working outward. The radial dimensions are shown in Table 1.

B.   HARTMAN INSPECTION RESULTS

1.   Alignment and Focal-Plane Establishment

Alignment of the polar graph used as a target with the optical axis is accomplished through simultaneous use of lights from each quadrant of the mirror. With the target set between the convergence point and the mirror at a distance sufficient to separate the images, the alignment is adjusted until the four light images form a symmetrical cross. The focal plane is then established by moving the target outward until the convergence point is reached. The criterion for establishment of the base-reference focal plane was the most tightly superimposed light pattern from the zone B holes. Figure 5 shows this pattern on the target photographically. The established focal length of the mirror was 69.17 in., which also established the rim angle θ of 44.79 deg.

During the iteration steps of the alignment procedure a broad sample scan of various parts of the mirror was made to generally locate any major warpage or distortion. A rather abrupt change in contour in the general region of the 91.8-in. diameter (zone G) was observed. The region outside this diameter focused irregularly in front of the base-reference focal plane ($f_{base\ ref}$ = 69.17) converging at a plane 68.23 in. from the parabola apex.

Four observed patterns are presented in Fig. 6 to illustrate sample data and the abrupt variation near the 7.5-ft diameter. These patterns are for the 99-deg angular position at the F, G, H, and I radial positions.

2.   Geometric Error and Geometric Efficiency Results

Data from the Hartman inspection are reduced into two forms: (1) the geometric characteristics of the mirror expressed in terms of the tangential error of the surface, and (2) the "geometric efficiency" characteristic with variable aperture sizes. (The geometric efficiency enables hypothetical performance curves, dependent on reflectivity, to be generated. When correlated with calorimeter test results these yield the "effective" surface reflectivity.)

Tangential error is broken down into three classifications, each derived directly from the individual observed target pattern (see Fig. 6). These are (1) parabolic profile error, (2) transverse (or circumferential) error, and (3) combined error. Data are presented for both the 9.5-ft-diam. full mirror and the 7.5-ft-diam. central portion. The 7.5-ft data are generally better on a specific basis and are probably a realistic limit of the optical quality attainable from the master. Table 2 presents the numerical data for the three error classifications. The same data are presented comparatively in Fig. 7, 8, and 9.

A contour map of the combined error is shown in Fig. 10. The zones of the mirror having a combined tangential error greater than 10 min are shaded. There are three major zones and two isolated spots in this category. The major zones correlate with the mounting points on the mirror torus. It is believed that much of this distortion resulted during shipping. Trouble with shipping-bracket breakage and mounting-bolt loosening in the crate was experienced.

Geometric efficiency vs aperture size was determined for the full 9.5-ft-diam. mirror and for the 7.5-ft-diam. central portion. A finite summation of the segments of each observed target pattern is performed to obtain the geometric efficiency. With this factor determined, only the reflectivity term in the cavity energy formula given below remains unknown. By supplying variable reflectivity values, a family of hypothetical cavity-energy performance curves is obtained from the optical inspection data. The data are then correlated with the observed cavity-energy results from the subsequent calorimeter tests and where qualitative correlation is obtained yield quantitative data concerning the effective surface reflectivity.

Cavity-Energy Formula

$Energy_{cavity}$

$$= \text{solar insolation } (\text{w/ft}^2) \times \text{area}_{intercept} \times \eta_{shadow} \times \eta_{reflect} \times \eta_{geom} \times \eta_{trans}$$

where

$$\text{solar insolation} = \text{as observed (standardized to 90 w/ft}^2 \text{ for curves)}$$

$$\text{area}_{intercept} = 70.882 \text{ ft}^2 \text{ for 9.5-ft-diam.}$$
$$= 44.179 \text{ ft}^2 \text{ for 7.5-ft-diam.}$$

$$\eta_{shadow} = 0.94925 \text{ for 9.5-ft-diam.}$$
$$= 0.92917 \text{ for 7.5-ft-diam.}$$

$$\eta_{geom} = \text{geometric efficiency for applicable aperture (Table 3)}$$

$$\eta_{trans} = \text{transmissivity factor for vacuum-chamber window} \\ (= 1.000 \text{ for calorimeter test used for correlation} \\ \text{since no window was used)}$$

$$\eta_{reflect} = \text{effective surface reflectivity}$$

Geometric efficiencies for each half of the mirror and for the overall mirror for each diameter are shown in Fig. 11. The overall efficiency factors are also tabulated in Table 3.

Figures 12 and 13 show the families of hypothetical cavity-energy performance curves for the 7.5-ft and 9.5-ft diameters respectively and also the subsequently obtained calorimeter curves used for the effective reflectivity correlation. Good correlation was obtained at the three largest apertures run with the calorimeter, and yielded consistent effective reflectivity results, as shown in Table 4.

The noncorrelation at the 0.625-in. cavity aperture is probably the result of the markedly increasing margin for experimental error with decreasing aperture sizes present in the optical-data reduction.

III. CALORIMETER TEST PROGRAM

A. TEST SETUP DESCRIPTION

A program of mirror-performance evaluation and calibration using cold calorimeter testing was performed with the 9.5-ft-diam. concentrator S/N 1. Elements of the test calorimeter are:

1. A 2-in.-ID by 2-in.-length water-cooled copper cup

2. Four interchangeable, independently cooled face plates varying only in the size of aperture opening

3. An asbestos insulating washer mounted between the face plate and cup to prevent energy exchange by conduction

Monitoring instrumentation includes:

1. Two Eppley Model 15 normal-incidence pyrheliometers, used to monitor solar insolation

2. Two pairs of differential thermocouples installed with cold junctions at the calorimeter-cup inlet cross and with hot junctions at the calorimeter-cup outlet cross

3. A digital voltmeter-recorder data-acquisition system for monitoring both pyrheliometers and one differential thermocouple

4. A millivolt potentiometer used to monitor the cross-check thermocouple

5. A flow-measuring system of the "balance-stop watch" type, using precision weights

6. Two ASTM 64F thermometers in the inlet and outlet lines used to cross-check the thermocouples and provide test operation guidance.

An overall view of the mirror-calorimeter system in operation is presented in Fig. 14. The focal-zone test installation (including the vacuum-chamber window) is shown nonoperating in Fig. 15 and operating in Fig. 16. A similar operating picture without the vacuum-chamber window is shown in Fig. 17.

B.   CALORIMETER TEST RESULTS

1.   Peak Thermal Power

Peak thermal power vs aperture-size testing was performed with both the "open" (no chamber window) and "windowed" focal-zone, configurations at exposed mirror diameters of both 9.5 and 7.5 ft. Figure 18 is an overall view of the test operating with the 7.5-ft-opening mask. The shadowed ring between the 7.5-ft and 9.5-ft diameters is clearly evident. Figure 19 is a view of the focal-zone setup operating during a test of the 7.5-ft-diam. portion.

Thermal bull's-eye was determined for each aperture by traverses along the optical axis and high-low-east-west disorientation traverses starting from the optical inspection bull's-eye. The bull's-eye position varied with aperture size over a distance of 0.100 in. axially and approximately ±3 min disorientation angle. The axial traverses are shown in Fig. 20 for each aperture size with the 9.5-ft-diam. mirror exposure. Both the open and windowed traverses are shown and illustrate the axial shift of the focused-energy bundle caused by the window optically, as well as the energy-level drop resulting from window reflection and transmissivity losses. The peaks on some of these curves were later exceeded during the disorientation search traverses.

Peak performance data are presented in terms of efficiency (based on the total intercepted area) in Fig. 21 for both the 9.5- and 7.5-ft diameters. Data for both the open and windowed test configurations are presented. The definite efficiency gain at the smaller mirror diameter is the result of the higher optical quality present in the central zone, as discussed in the Hartman test results in Sect. IIB.

Direct comparison of this mirror with mirrors of other sizes and rim angles may be made from the data in Fig. 22, in which the "reflecting surface efficiency" is plotted against the "exposed reflective surface/aperture" area ratio. The reflecting surface efficiency is defined as the concentrator efficiency (intercepted area) divided by the shadow factor. This term is used to enable generalization of the curve, eliminating the differences caused by variations in the shadow from setup to setup. The exposed reflecting surface/aperture area ratio is used in place of the more common concentration ratio for the same reason. Examination of Fig. 22 reveals that on the generalized basis the 7.5-ft-diam. central portion outperformed the full mirror only at area ratios below 11,000. Above this the curves are essentially coincident.

Thermal power reflected from the mirror, received through the vacuum chamber window, and retained in the generator after compensating for the aperture radiation loss at 2000°K is shown in Fig. 23 for the 9.5-ft-diam. mirror operating at ground-test conditions of 90 w/ft^2. Corresponding numerical data are included in Table 5.

Comparable thermal-power data for the 7.5-ft-diam. central portion are plotted in Fig. 24 and shown numerically in Table 6. It will be noted that in Fig. 23 (full mirror) the optimum aperture size for a generator was just being approached at 1.400 in., while with the smaller mirror exposure the optimum was near 1.000 in.

Six corresponding runs with different aperture sizes or mirror sizes were obtained where a transmissivity efficiency η_{trans} for the quartz vacuum-chamber window could be directly derived. These results are shown in Table 7. This is slightly better than the 0.8902 obtained with the same window using a 60-deg-rim-angle mirror, and is probably a real improvement caused by the more normal angle of incidence of the impinging energy from the mirror.

To further explore the optimum aperture-shift characteristic with variations in the energy level, data were converted to the space solar intensity (with the vacuum-chamber window loss deleted, as the window is only a ground-test component) and plotted on Fig. 25. Corresponding numerical data are tabulated in Tables 8 and 9.

With the 7.5-ft-diam. portion of the mirror exposed, the optimum generator aperture shifted upward approximately 0.200 in. in diameter from 1.000 to 1.200, when the energy level was increased from the 90 w/ft^2 ground-test level to the 130 w/ft^2 space solar-intensity level. The optimum was still rising with the 9.5-ft mirror at the largest aperture tested, hence a shift is evident, but its magnitude could not be determined from the available data.

2.   Disorientation

Disorientation performance was obtained only with the full-mirror test setup. Complete data at each aperture for 6 and 12 min at high, low, east, and west disorientation were obtained using the quartz window. A set of data for the 1.000-in. aperture was also obtained with the open configuration. Data are presented in the form of percent of bull's-eye power in Fig. 26 and Table 10.

It will be noted that the 1.400-in.-aperture configuration has the best performance (minimum drop-off rate) with disorientation, making it the optimum configuration from a thermal-performance standpoint in two categories: (1) attaining the highest net energy available to the converters (see Fig. 23 and Table 5), and (2) having the highest degree of preservation of the peak power with disorientation. A partial set of disorientation data obtained with the 7.5-diam. portion of the mirror is presented in Table 11. Calorimetry data for the 9.5-ft-diam. mirror are summarized in Table 12.

A bar graph of the focal-plane flux pattern is given in Fig. 27 for comparison with future mirrors having similar and different geometric configurations. The pattern felt by the generator in the chamber is shown, together with the open pattern at the ground-test solar intensity of 90 w/ft^2 and the open pattern that would result at the space solar-intensity level of 130 w/ft^2.

IV. CONCLUSIONS

1. Overall quality of the mirror is high, enabling its use as a power source for thermionic generators having a wide range of cavity aperture sizes.

2. Performance gains can be obtained in subsequent mirrors made from the same master through corrective attention in the following two detail categories:

      a.   Improvement in the surface finish and effective reflectivity

      b.   Handling (the major distortion-limiting performance of the present mirror occurred after the mirror had been parted from the master, probably during shipment)

3. From a system viewpoint this mirror will yield the greatest amount of convertible energy (2000°K temperature level) to a generator sized around a 1.400-in. aperture and minimum cavity diameter.

Table 1. Radial positioning of the holes
in the Hartman screen

Position	Radius, in.
A	12.745
B	22.075
C	28.499
D	33.721
E	38.236
F	42.271
G	45.954
H	49.362
I	52.550
J	55.556

Table 2. Geometric quality of 9.5-ft-diam. concentrator S/N 1

| Tangential error, min | Percent of mirror area equal to or better than error value | | | | | |
| | Parabolic profile | | Transverse | | Combined | |
	7.5-ft-diam.	9.5-ft-diam.	7.5-ft-diam.	9.5-ft-diam.	7.5-ft-diam.	9.5-ft-diam.
±1	18.8	13.5	31.2	25.5	3.21	2.5
±2	31.6	24.5	53.6	44.0	13.0	9.5
±3	48.2	38.5	74.6	62.0	30.2	23.5
±4	68.6	52.5	84.6	70.5	50.6	37.5
±5	78.0	61.0	89.6	78.0	64.8	50.5
±6	86.0	67.0	90.6	81.5	73.0	56.5
±7	88.8	69.5	95.6	84.5	79.8	63.0
±8	93.6	75.5	97.2	87.0	89.4	70.0
±9	95.6	79.0	97.6	88.5	93.0	75.5
±10	96.4	80.0	98.4	90.0	94.6	77.5
±11	99.0	83.5	98.4	91.5	98.2	81.5
±12	99.0	84.5	98.4	93.0	98.2	82.0
±13	99.2	86.5	98.4	93.0	99.0	83.5
±14	99.2	87.0	99.2	93.5	99.2	85.0
±15	99.2	87.5	99.2	94.5	99.2	85.5

Table 3. Geometric efficiency factors vs aperture diameter
of the 9.5-ft-diam. mirror S/N 1

Aperture diameter, in.	7.5-ft-diam. central portion	9.5-ft-diam. full mirror
0.600	0.4577	0.3568
0.800	0.6856	0.5402
1.000	0.8347	0.6688
1.200	0.9169	0.7473
1.400	0.9580	0.7971
1.600	0.9809	0.8299
1.800	0.9906	0.8508
2.000	0.9966	0.8707

Table 4. Effective reflectivity from Hartman-calorimeter data correlation

Aperture diameter, in.	Effective surface reflectivity[a]	
	7.5-ft-diam. data correlation	9.5-ft-diam. data correlation
0.825	0.8071	0.8258
1.000	0.8333	0.8143
1.400	0.8019	0.8167

[a]Overall average reflectivity (6 points above) = 0.8165

Table 5. Thermal power--9.5-ft-diam., 90 w/ft^2 ground-test solar intensity

Parameter	0.625-in. aperture (concentration ratio = 33,270)	0.825-in. aperture (concentration ratio = 19,094)	1.000-in. aperture (concentration ratio = 12,996)	1.400-in. aperture (concentration ratio = 6,631)
Peak power, w Open calorimeter	2192.6	2787.8	3298.3	3942.8
Peak efficiency Open calorimeter	0.3437	0.4370	0.5170	0.6180
Peak power, w Windowed (through quartz)	1982.2	2487.0	3002.3	3581.6
2000°K black-body radiation loss, w	179.5	312.8	459.6	900.7
Net generator energy available for conversion	1802.7	2174.2	2542.7	2680.9

Table 6. Thermal power--7.5-ft-diam., 90 w/ft^2 ground-test solar intensity

Parameter	0.625-in. aperture (concentration ratio = 20,736)	0.825-in. aperture (concentration ratio = 11,900)	1.000-in. aperture (concentration ratio = 8,100)	1.400-in. aperture (concentration ratio = 4,133)
Peak power, w Open calorimeter	1663.8	2102.2	2515.0	2838.1
Peak efficiency Open calorimeter	0.4185	0.5287	0.6325	0.7138
Peak power, w Windowed (through quartz)	1481.1	1871.5	2311.5	2578.2
2000°K black-body radiation loss, w	179.5	312.8	459.6	900.7
Net generator energy available for conversion, w	1301.6	1558.7	1851.9	1677.5

Table 7. η_{trans} derivation data[a]

Aperture diameter	Mirror diameter exposed, ft	Open calorimeter peak, w	Cavity peak through quartz, w	η_{trans}
0.625	9.5	2192.6	1982.2	0.9040
0.825	7.5	2102.2	1871.5	0.8902
0.825	9.5	2787.8	2487.0	0.8920
1.000	7.5	2515.0	2311.5	0.9191
1.000	9.5	3298.3	3002.3	0.9102
1.400	9.5	3942.8	3581.6	0.9084
[a]Average η_{trans} (from 6 above) = 0.9040				

Table 8. Thermal power--9.5-ft-diam., 130 w/ft^2 space solar intensity

Parameter	0.625-in. aperture	0.825-in. aperture	1.000-in. aperture	1.400-in. aperture
Peak efficiency Open calorimeter	0.3437	0.4370	0.5170	0.6180
Thermal power at space solar flux, w	3167.1	4026.8	4764.0	5694.7
2000° K black-body radiation loss, w	179.5	312.8	459.6	900.7
Net generator energy available for conversion, w	2987.6	3714.0	4304.4	4794.0

Table 9.   Thermal power--7.5-ft-diam., 130 w/ft^2 space solar intensity

Parameter	0.625-in. aperture	0.825-in. aperture	1.000-in. aperture	1.400-in. aperture
Peak efficiency Open calorimeter	0.4185	0.5287	0.6325	0.7138
Thermal power at space solar flux, w	2403.6	3036.5	3632.6	4099.6
2000°K black-body radiation loss, w	179.5	312.8	459.6	900.7
Net generator energy available for conversion, w	2224.1	2723.7	3173.0	3198.9

Table 10.   Disorientation performance--9.5-ft-diam. mirror exposure[a]

Test setup configuration	Bull's-eye efficiency	6 min disorientation		12 min disorientation	
		Efficiency	% of bull's-eye	Efficiency	% of bull's-eye
0.625-in. aperture	0.3107	0.2930	94.30	0.2501	80.49
0.825-in. aperture	0.3898	0.3631	93.15	0.3059	78.48
1.000-in. aperture	0.4706	0.4500	95.63	0.3963	84.21
1.400-in. aperture	0.5614	0.5496	97.90	0.5119	91.19

[a]Results are averages of individual high, low, east, and west disorientation data (Table 12).

Table 11. Calorimetry data summary--7.5-ft-diam. opening mirror mask

	0.625 in. Aperture			0.825 in. Aperture			1.000 in. Aperture			1.400 in. Aperture		
	Run No.	Efficiency	Std. watts	Run No.	Efficiency	Std. watts	Run No.	Efficiency	Std. watts	Run No.	Efficiency	Std. watts
F^a + 0.100 in. Open Bull's-eye	425-426	0.4185	1663.80	437-439 427-428 431-433 Average	0.5288 0.5308 0.5264 0.5287	2102.56 2110.71 2093.02 2102.2	380-381 384-385 389-390 397-398 Average	0.6157 0.6188 0.6214 0.6161 0.6188	2448.1 2460.4 2470.7 2449.7 2460.4	399-400 407-408 409 414-415 Average	0.6906 0.7063 0.7122 0.7228 0.7138	2745.89 2808.32 2831.8 2873.9 2838.14
6 min High	419-421 416	0.4105 0.4136	1632.2 1644.5				390-391	0.5824	2315.7	412-413	0.7183	2856.03
6 min Low	422-423	0.4168	1657.2	434			386-388	0.6076	2415.9	410-411	0.7073	2812.29
6 min East				430	0.4712	1873.54	395-396	0.6025	2395.6	403-404	0.6973	2772.53
6 min West				429	0.5035	2001.97	393-394	0.5845	2324.0	401-402	0.6831	2716.07
										405-406	0.6893	2740.92
F +0.500 in. Quartz Bull's-eye				440-443	0.4707	1871.55	453-455 460-461 Average (Incl. 458-459)	0.5825 0.5754 0.5811	2316.08 2287.85 2311.5			
6 min High												
6 min Low												
6 min East												
6 min West												
F +0.400 in. Quartz							458-459	0.5853	2327.4			
F +0.600 in. Quartz							456-457	0.5598	2225.8			
F +0.100 in. Open Bull's-eye							444-446 449-450 451-452 Average	0.6353 0.6426 0.6501 0.6463	2526.0 2555.0 2584.9 2569.7			

[a] Focal plane.

Table 12. Calorimetry data summary--9.5-ft-diam. mirror

Test Configuration	0.625-in. Aperture			0.825-in. Aperture			1.000-in. Aperture			1.400-in. Aperture		
	Run No.	Efficiency	Std. watts	Run No.	Efficiency	Std. watts	Run No.	Efficiency	Std. watts	Run No.	Efficiency	Std. watts
F[a] -0.300 in. Open				230-231	0.3695	2357.5				179-180	0.6061	3866.6
F -0.200 in. Open				232-233	0.3951	2520.8	121-123	0.5016	3199.6	177-178	0.6103	3893.3
F -0.100 in. Open				234-235	0.4138	2640.1	118-120	0.5090	3247.1	175-176	0.6189	3948.2
F Open	124-126 136	0.3248 0.3297	2072.0 2103.4	224-225 228-229 236-237	0.4248 0.4201 0.4157	2710.3 2680.3 2651.6	115-117	0.5170	3298.3	171-174 181-182	0.6178 0.6183	3941.0 3944.7
F +0.100 in. Open	127-129 348-350	0.3294 0.3437	2101.1 2192.6	238-239 291-292	0.4213 0.4370	2687.9 2787.8	112-114 354-355 360-361 367-368 373-374	0.5157 0.5149 0.5163 0.5181 0.5187	3289.7 3285.1 3293.7 3305.5 3309.0	183-184	0.6132	3911.8
F +0.200 in. Open	130-132	0.3246	2070.9	240-241	0.4148	2669.5	109-111	0.5103	3255.6	185-186	0.6000	3827.96
F +0.300 in. Open	133-135	0.3149	2009.1	242-243	0.4015	2561.3				187-188	0.5898	3762.6
F +0.400 in. Open												
F Quartz	137-139	0.2567	1637.6									
F +0.100 in. Quartz	140-142	0.2740	1748.1							189-190	0.5450	3480.0
F +0.200 in. Quartz	143-145 167	0.2888 0.2959	1842.1 1887.6	261-262	0.3678	2346.3	106-108	0.4573	2917.0	191-192	0.5570	3553.6
F +0.300 in. Quartz	146-148 165-166	0.2989 0.3047	1908.8 1944.1	259-260	0.3763	2400.5	103-105	0.4688	2990.7	193-194	0.5314	3561.4
F +0.400 in. Quartz	149-152 163-164	0.3065 0.3088	1955.3 1969.9	244-246 257-258	0.3836 0.3843	2447.3 2451.9	98-100 101-102	0.4685 0.4701	2988.5 2998.6	195-197 208-209 218-219	0.5618 0.5617 0.5608	3583.9 3583.6 3577.6

Position	Reading			Reading			Reading			Reading		
F +0.500 in. Quartz	342-343 336-337 153-155 161-162 324-325 330-331	0.3139 0.3145 0.3062 0.3083 0.3070 0.3091	2002.5 2006.6 1953.6 1967.1 1960.0 1958.8 1972.2	285-286 276-278 247-249 255-256 263 264-265 270-271	0.3886 0.3911 0.3860 0.3934 0.3826 0.3857 0.3871	2479.3 2495.1 2462.2 2510.0 2440.5 2460.9 2469.5	89- 91 297-298 303-304 309-310 315-316	0.4679 0.4738 0.4715 0.4715 0.4684	2984.9 3022.9 3007.9 3007.9 2988.4	198-199	0.5539	3533.9
F +0.600 in. Quartz	156-158 159-160	0.3014 0.3028	1922.7 1932.0	250-252	0.3815	2433.5				200-201	0.5496	3505.8
F +0.700 in. Quartz				253-254	0.3774	2407.6				202-203	0.5322	3395.4
6 min High Quartz	332-333	0.2772	1768.7	287-288	0.3559	2270.4	305-306 (363-364)[b]	0.4584 (0.5027)	2924.3 (3207.2)	206-207	0.5590	3566.1
6 min Low Quartz	328-329	0.3075	1961.7	283-284	0.3686	2351.4	301-302 (358-359)	0.4424 (0.4840)	2822.6 (3087.9)	210-211	0.5391	3439.5
6 min East Quartz	344-345	0.2964	1890.8	272-273	0.3465	2210.6	317-318 (375-376)	0.4507 (0.4990)	2875.5 (3183.3)	216-217	0.5549	3540.2
6 min West Quartz	340-341	0.2911	1856.8	268-269	0.3816	2434.7	313-314 (371-372)	0.4486 (0.4951)	2861.8 (3158.4)	220-221	0.5456	3480.3
12 min High Quartz	334-335	0.2295	1464.1	289-290	0.3003	1915.7	307-308 (365-366)	0.4062 (0.4458)	2591.3 (2843.9)	204-205	0.5377	3430.2
12 min Low Quartz	326-327	0.2720	1735.5	281-282	0.3159	2015.6	299-300 (356-357)	0.3851 (0.4160)	2457.0 (2654.1)	212-213	0.4887	3117.9
12 min East Quartz	346-347	0.2544	1623.2	274-275	0.2840	1812.1	319-320 (377-378)	0.3985 (0.4369)	2542.3 (2787.5)	214-215	0.5118	3265.3
12 min West Quartz	338-339	0.2446	1560.4	266-267 279-280	0.3231 0.3062	2061.2 1953.3	311-312 (369-370)	0.3953 (0.4313)	2522.1 (2751.7)	222-223	0.5096	3251.3

[a] Focal plane.

[b] Numbers in parens are corresponding readings with open calorimeter in position F +0.100 in.

Fig. 1.   9.5-ft-diam., 45-deg-rim-angle electroformed solar concentrator S/N 1 during installation

Fig. 2.   Solar tracker structure prior to installation of 9.5-ft-diam. concentrator S/N 1
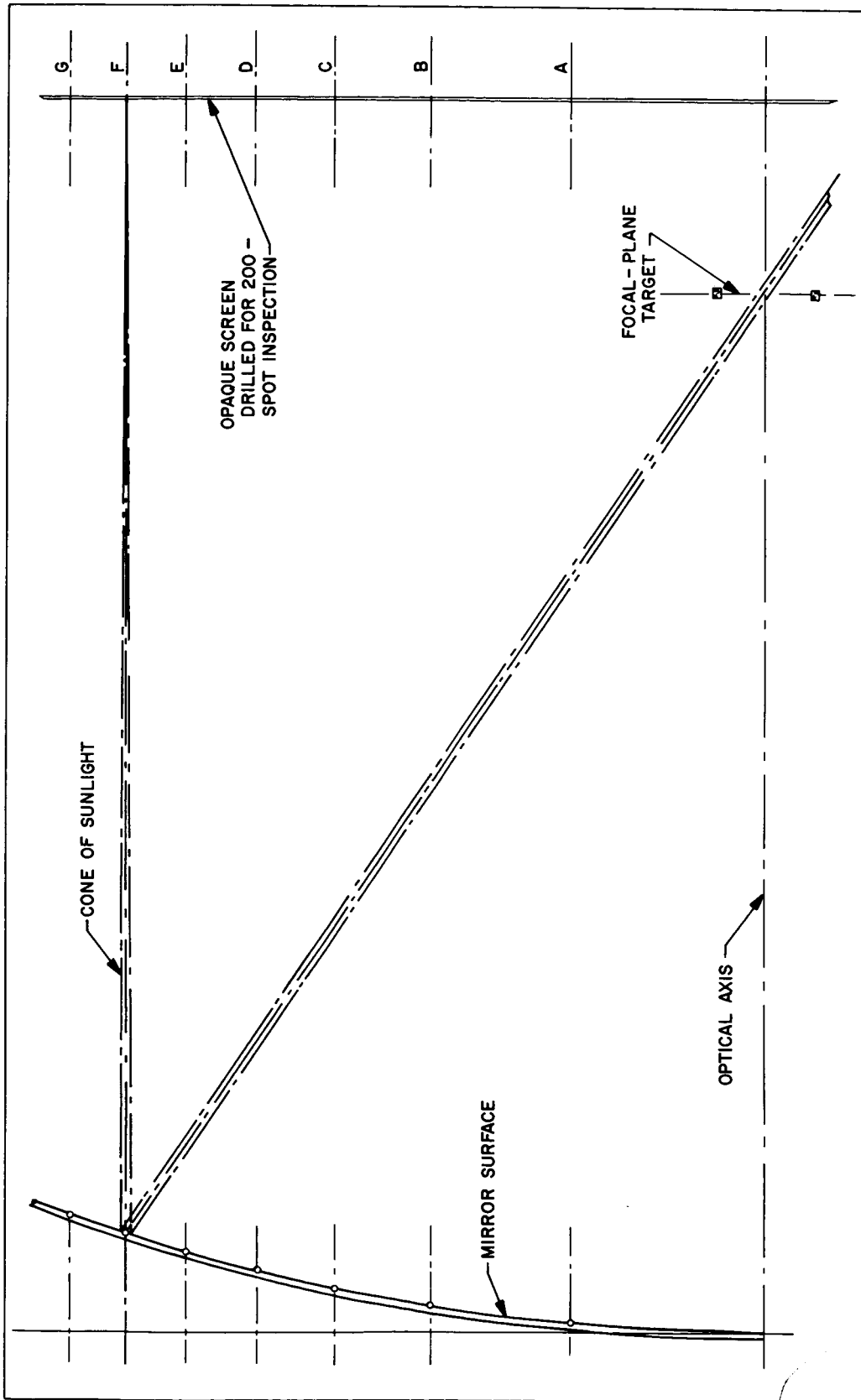
Fig. 3. Hartman inspection schematic
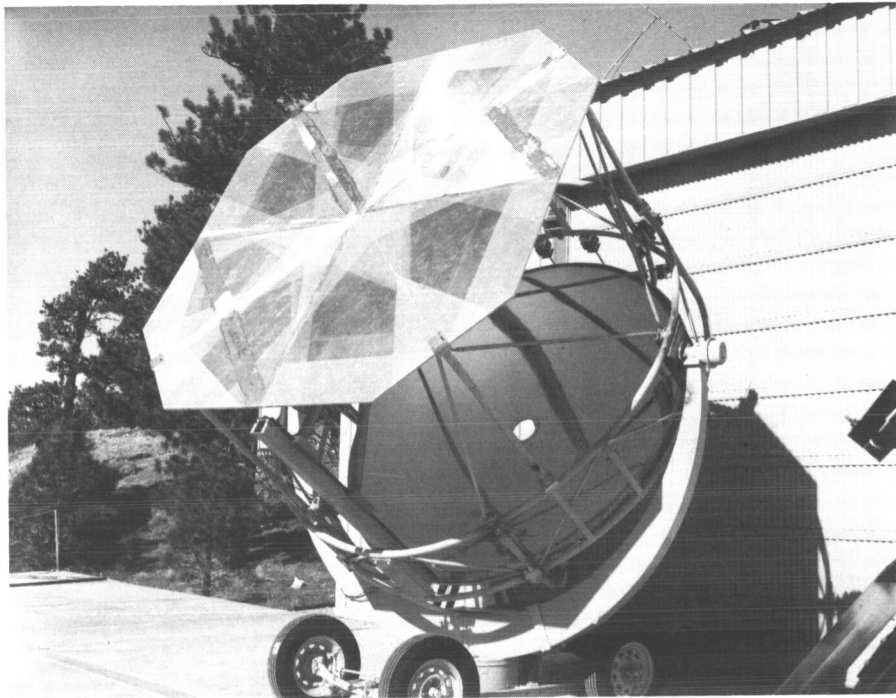
Fig. 4.   Hartman inspection test in operation--
concentrator S/N 1
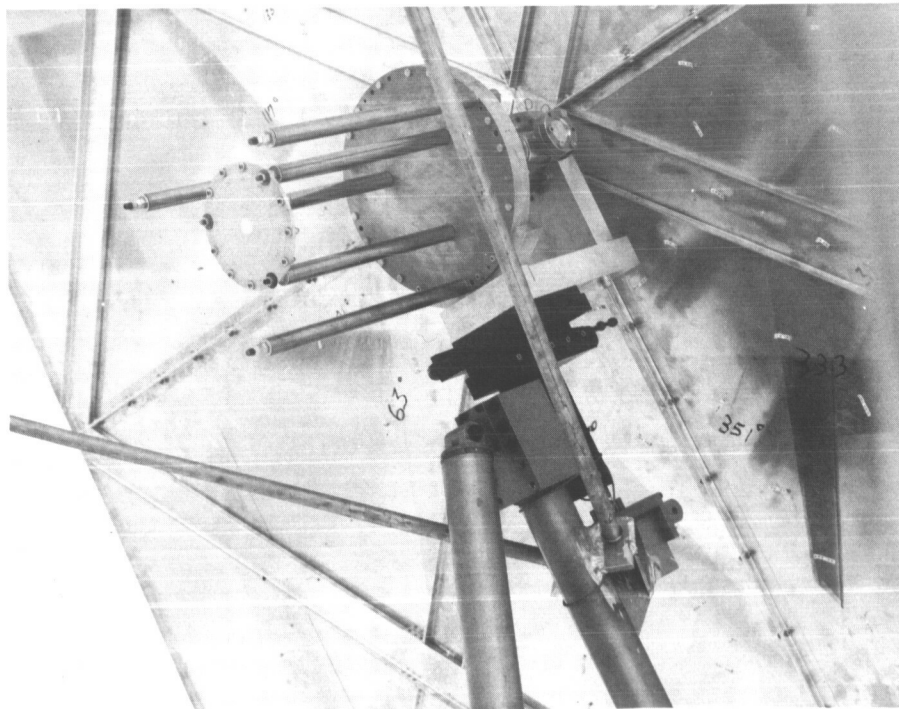
Fig. 5. Superimposed light pattern from four zone B
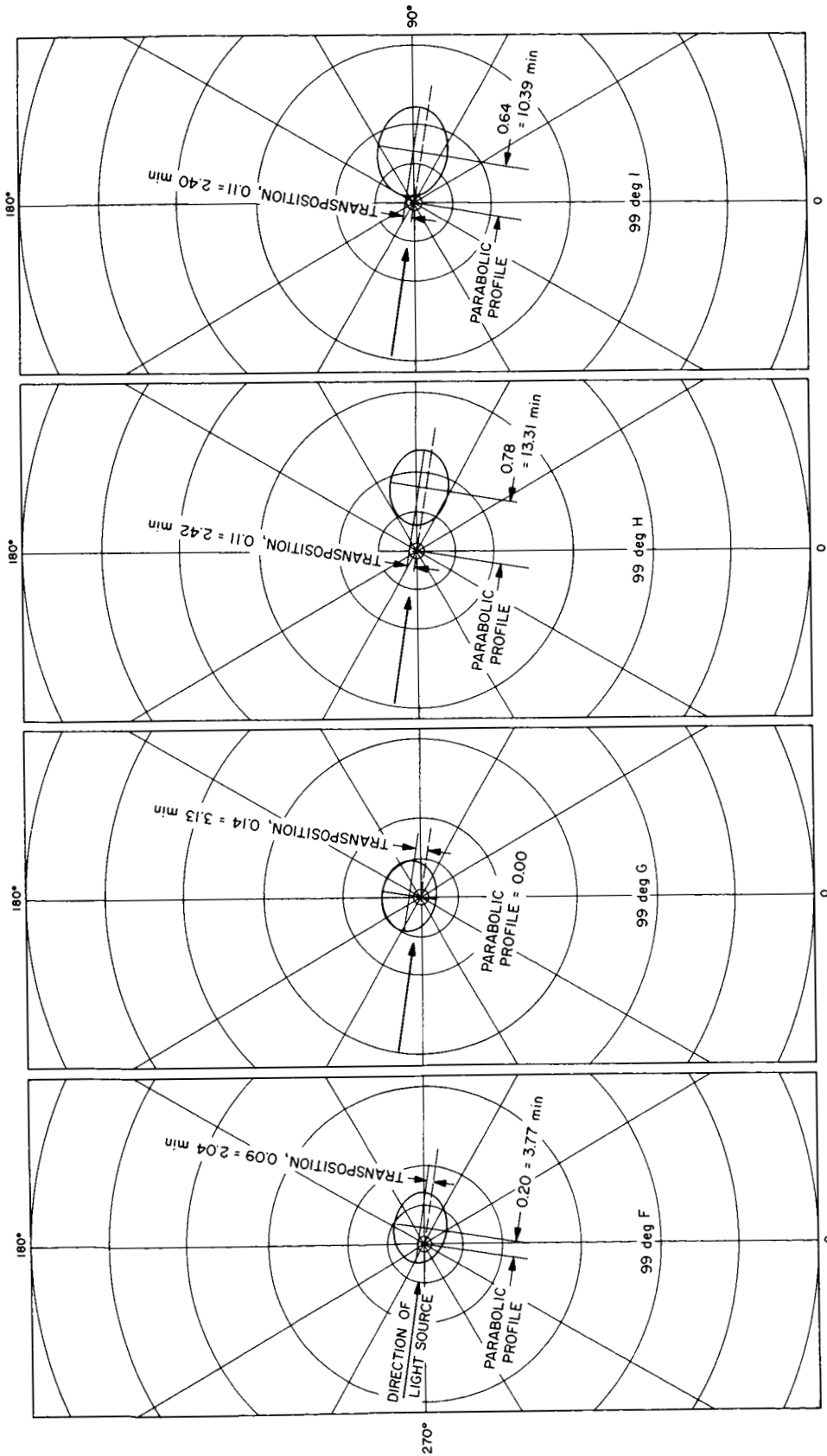holes establishing reference focal plane

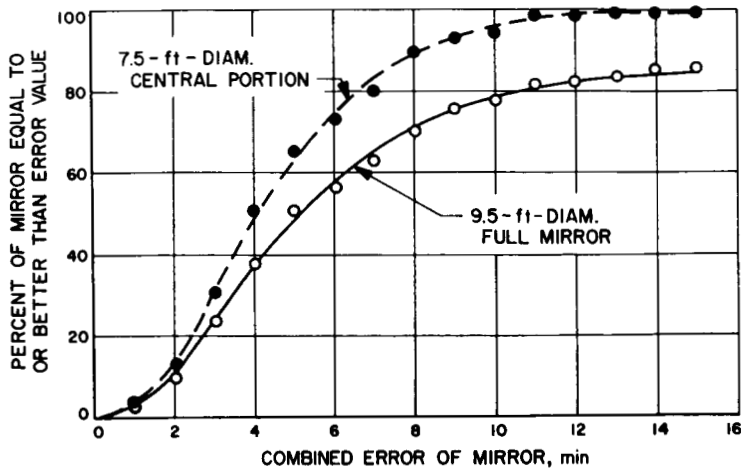Fig. 6. Four observed Hartman patterns illustrating typical contour change near the 7.5-ft diameter

Fig. 7. Combined tangential error comparison--7.5- and 9.5-ft diam.

Fig. 8. Parabolic profile tangential error comparison--7.5- and 9.5-ft-diam.
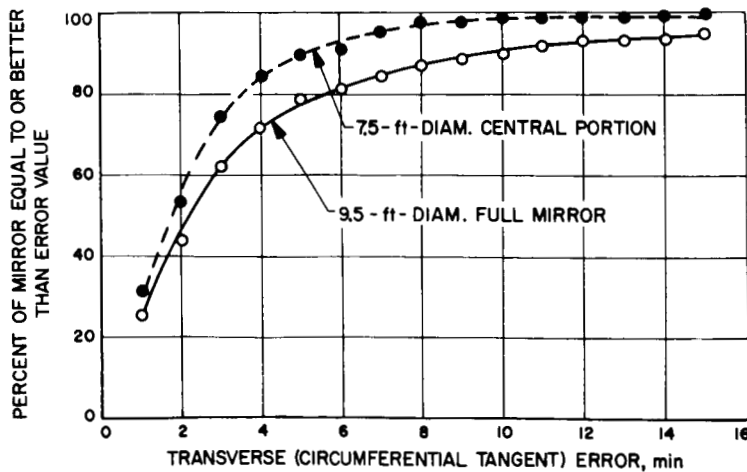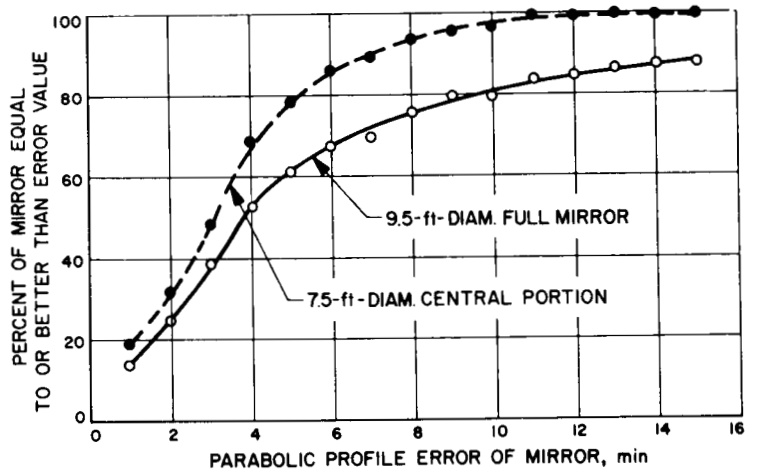
Fig. 9. Transverse tangential error comparison--7.5- and 9.5-ft-diam.
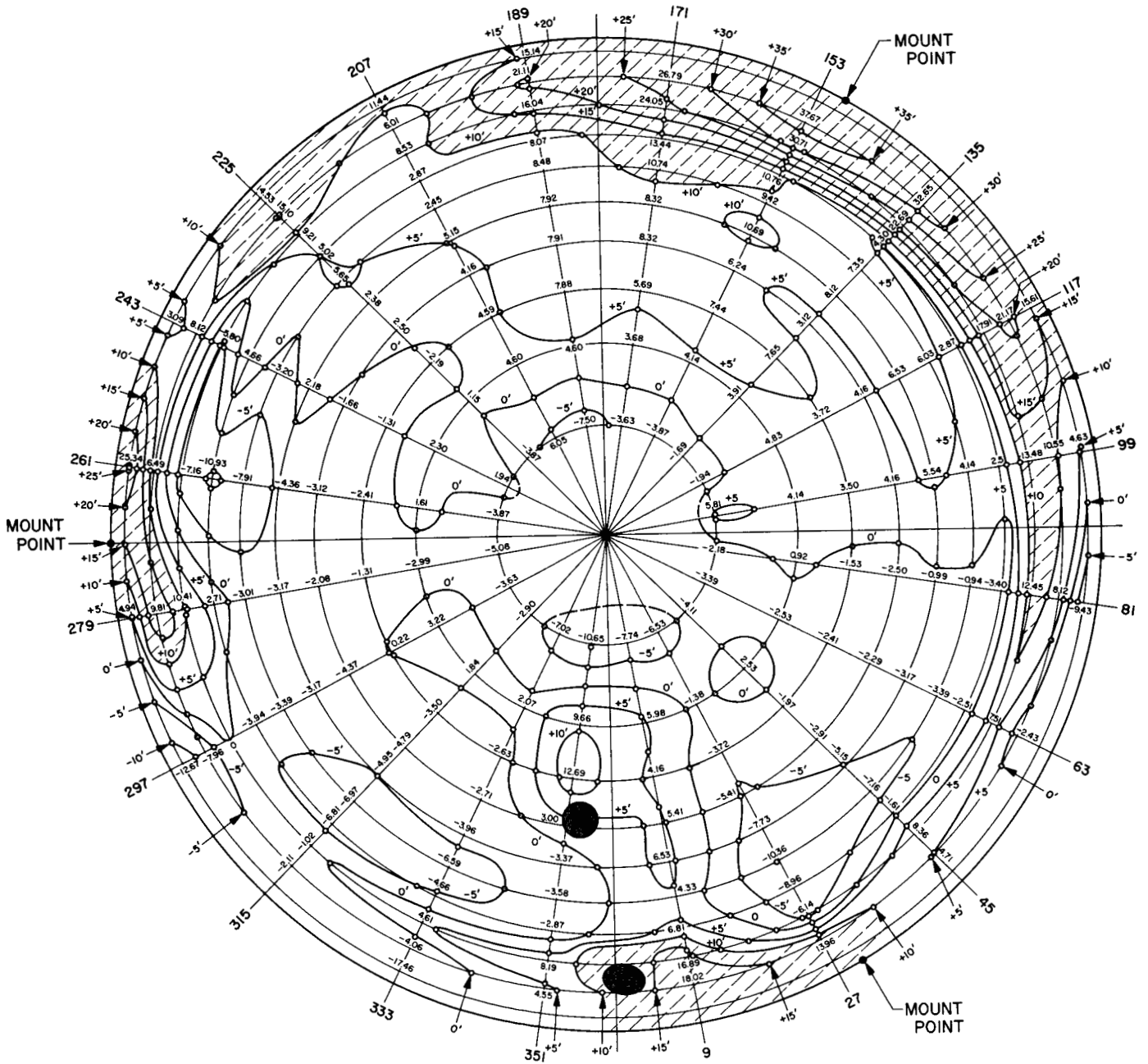
Fig. 10. Contour map of combined tangential error--9. 5-ft-diam.
(+ = deep dish; - = shallow dish)
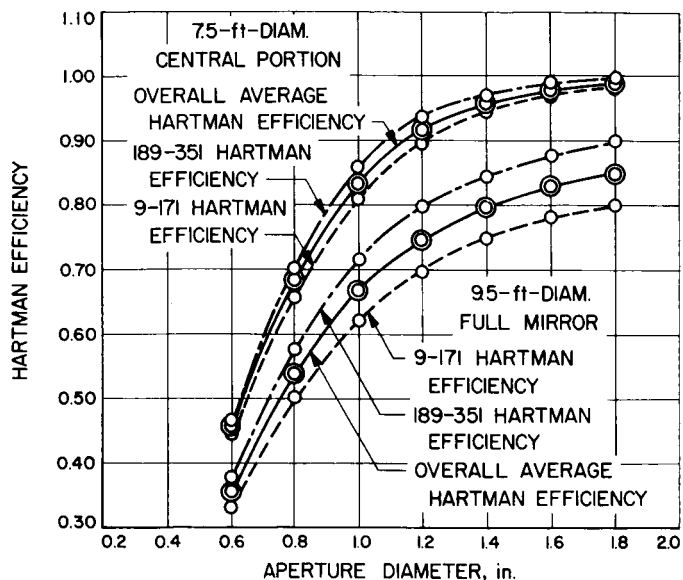
Fig. 11. Geometric efficiency factors--
7.5-ft- and 9.5-ft-diam.
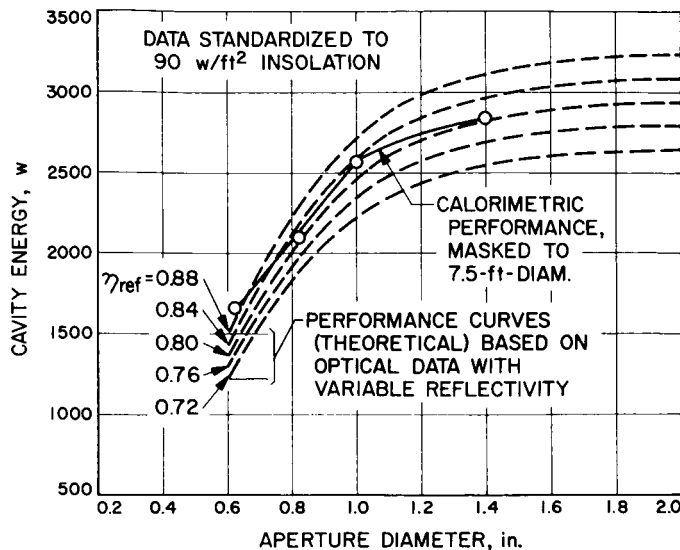
Fig. 12. Optical inspection correlation
of theoretical performance vs calori-
metric performance for the
7.5-ft-diam.
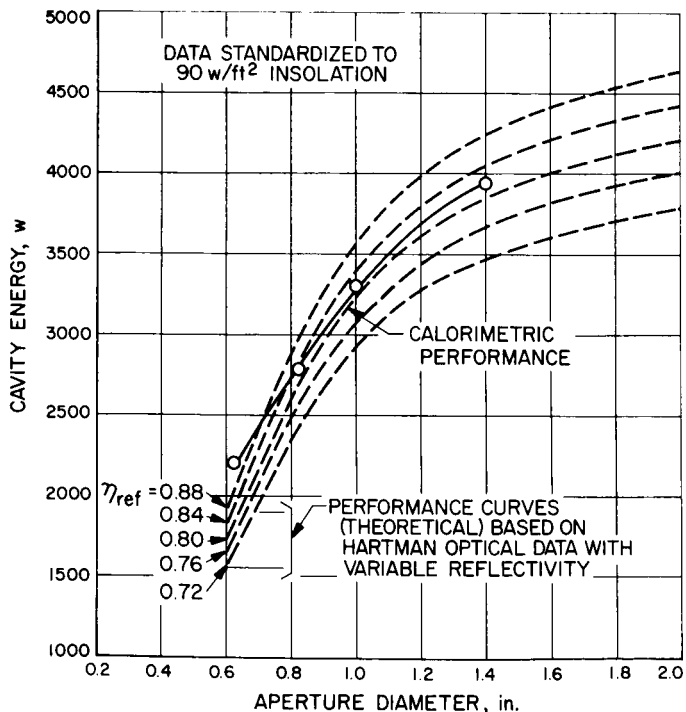
Fig. 13. Optical inspection correlation of
theoretical performance vs calorimetric
performance for the 9.5-ft-diam.

Fig. 14.   Calorimeter test in operation
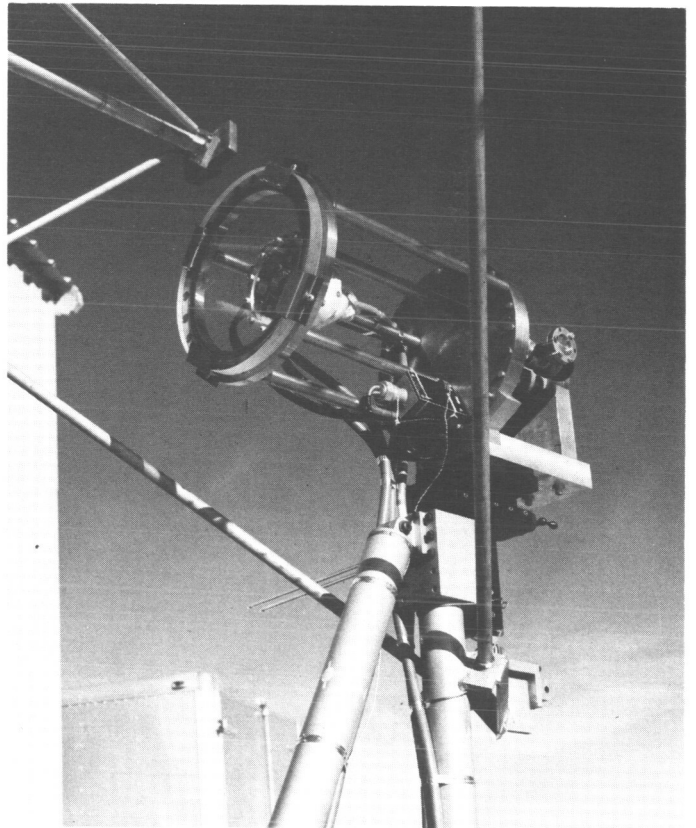
Fig. 15.   Calorimeter test focal-zone
setup, nonoperating

Fig. 16.   Calorimeter test focal-zone setup, windowed, operating

Fig. 17.   Calorimeter test focal-zone setup, open, operating

Fig. 18. 7.5-ft-diam.-opening mirror-mask calorimeter test in operation

Fig. 19. Calorimeter test focal-zone setup, operating with 7.5-ft-diam.-opening mirror mask
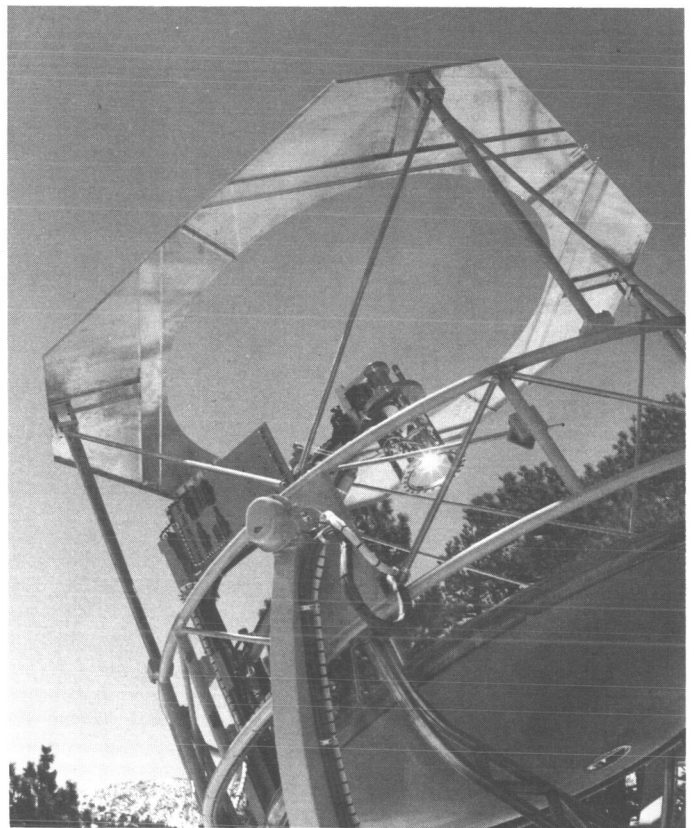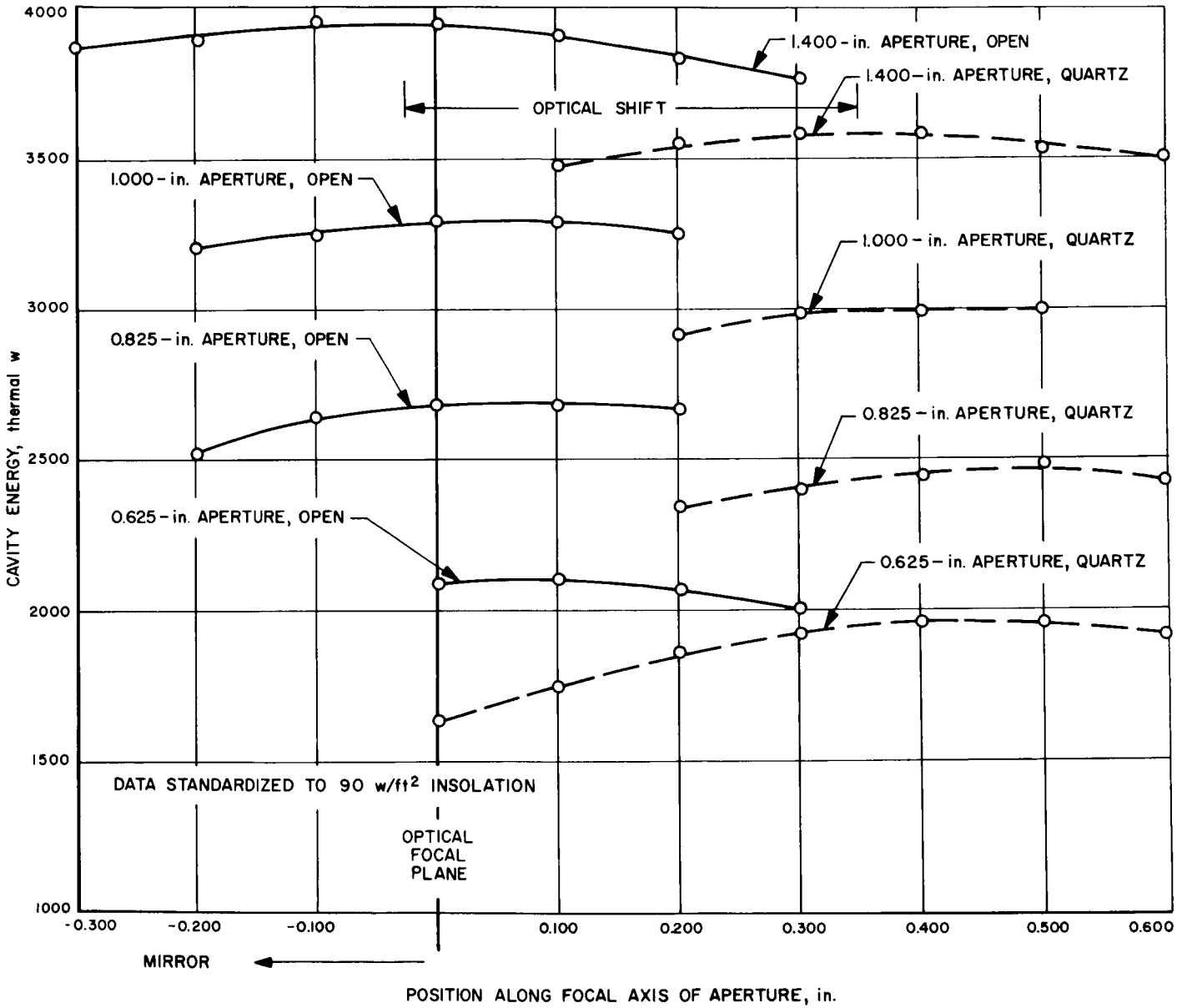
Fig. 20. Axial calorimeter traverses, open and windowed
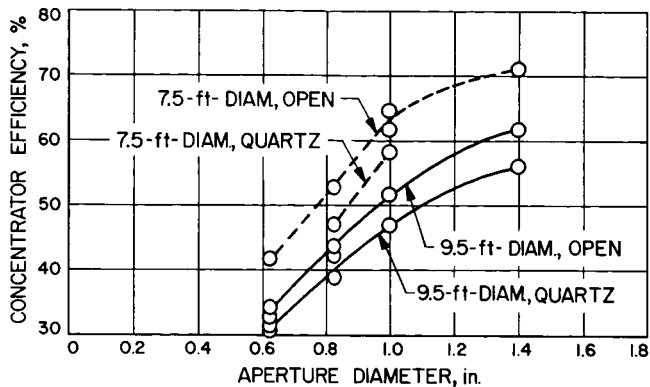
Fig. 21.   Mirror efficiency vs aperture size--7.5- and 9.5-ft-diam.
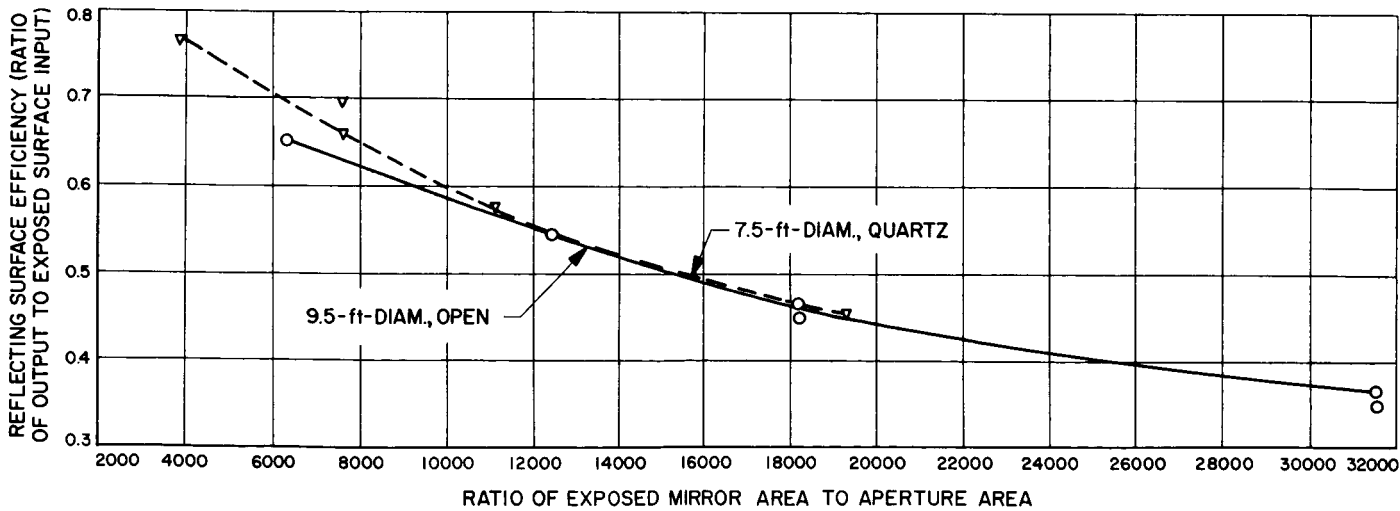
Fig. 22.   Reflecting surface efficiency vs area ratio
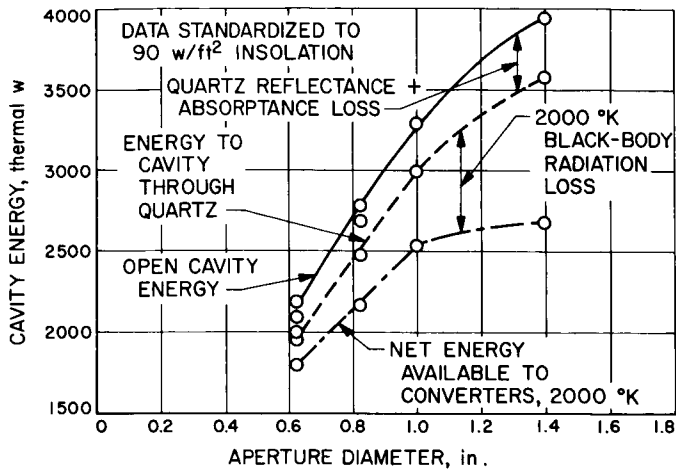
Fig. 23. Thermal power curves--
9.5-ft-diam., ground test
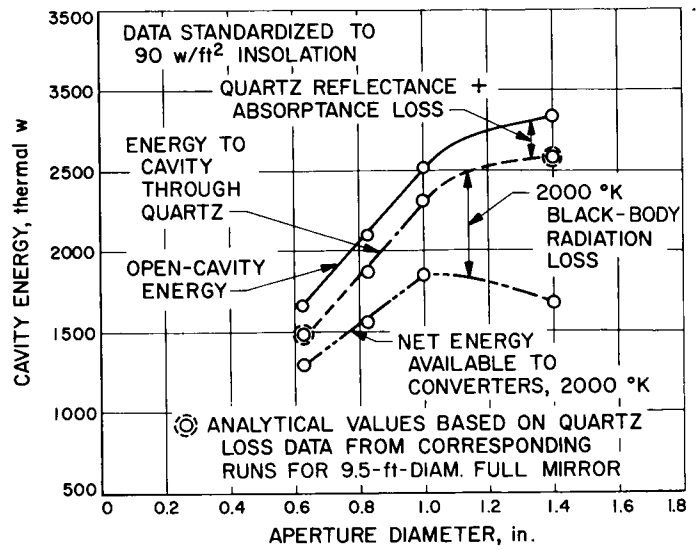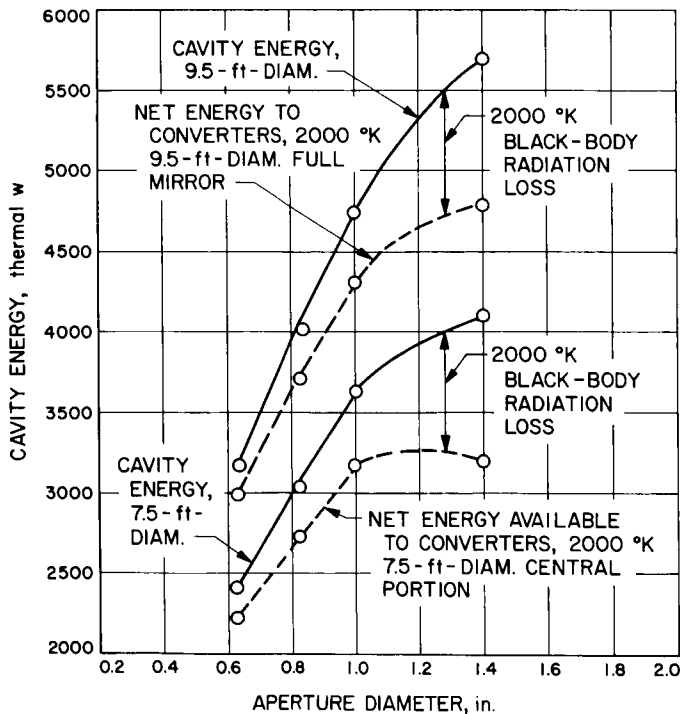
Fig. 24. Thermal power curves--
7.5-ft-diam., ground test

Fig. 25. Thermal power curves--
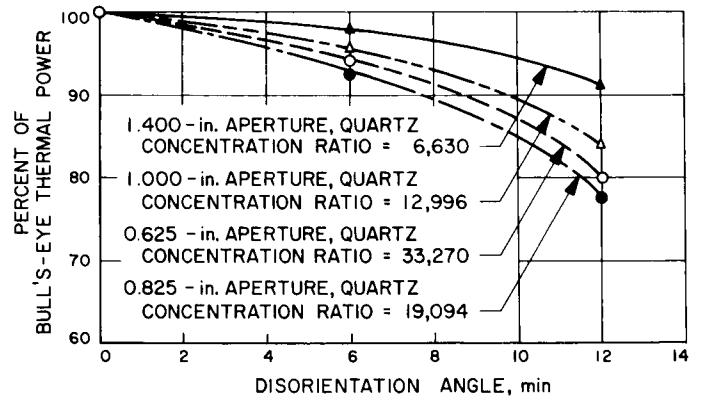9.5- and 7.5-ft-diam., extrapolated
to 130 w/ft^2 space insolation

Fig. 26. Disorientation performance
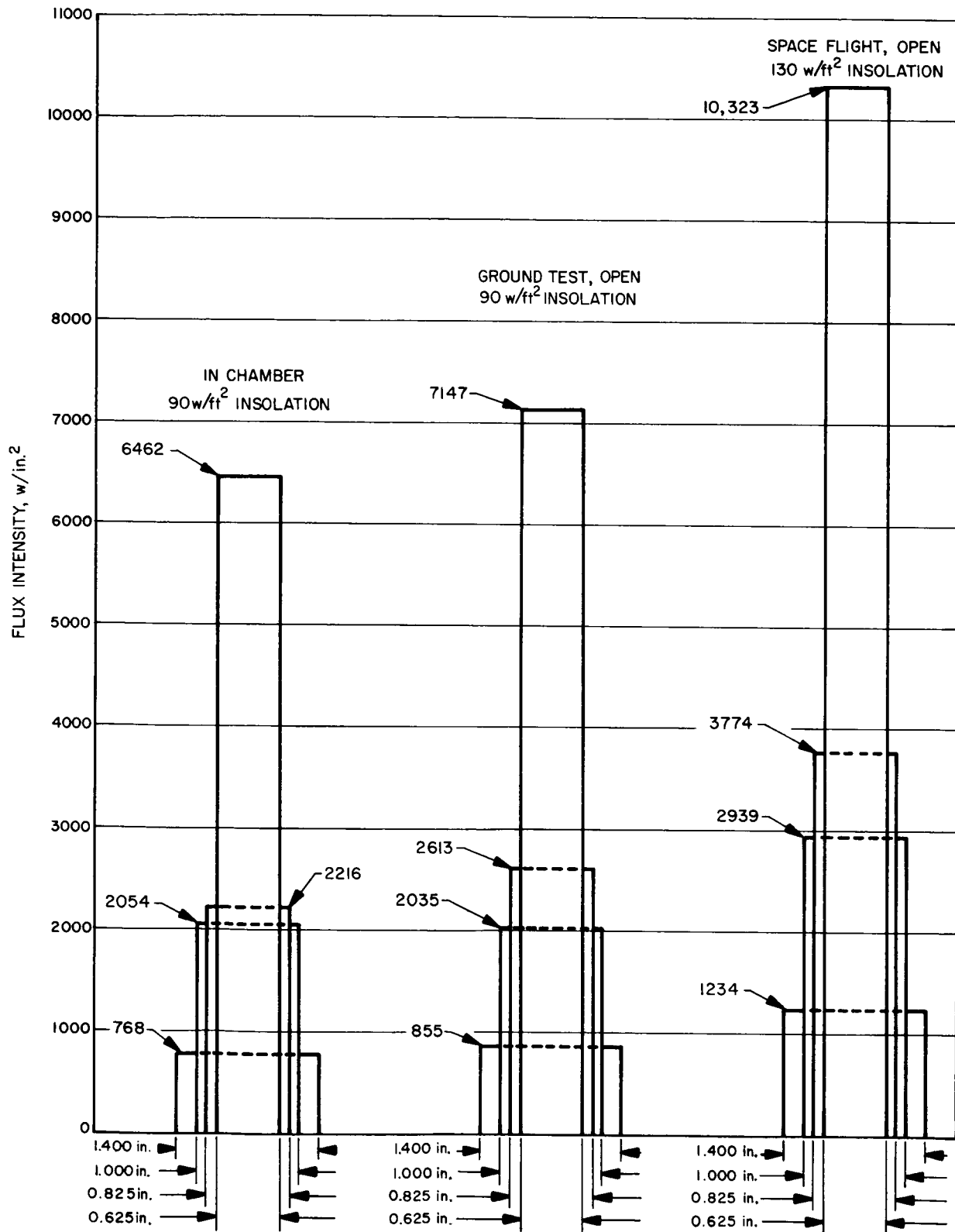with variable concentration ratios

Fig. 27. Focal-plane flux patterns as a function of cavity aperture: in chamber; ground test, open; space, open